crystals

MDPI

Article

Analysis of Thermal Effects in Kilowatt High Power Diamond Raman Lasers

Qiaoxia Gong [1], Mengxin Zhang [1], Chaonan Lin [1], Xun Yang [1], Xihong Fu [2], Fengying Ma [1], Yongsheng Hu [1,*], Lin Dong [1,3] and Chongxin Shan [1,3,*]

[1] Key Laboratory of Materials Physics of Ministry of Education, School of Physics and Microelectronics, Zhengzhou University, Zhengzhou 450001, China
[2] State Key Laboratory of Luminescence and Applications, Changchun Institute of Optics Fine Mechanics and Physics, Chinese Academy of Sciences, Changchun 130033, China
[3] Henan Key Laboratory of Diamond Optoelectronic Materials and Devices, School of Physics and Microelectronics, Zhengzhou University, Zhengzhou 450052, China
* Correspondence: huyongsheng@zzu.edu.cn (Y.H.); cxshan@zzu.edu.cn (C.S.)

Abstract: Chemical vapor deposition (CVD) diamond crystal is considered as an ideal material platform for Raman lasers with both high power and good beam quality due to its excellent Raman and thermal characteristics. With the continuous development of CVD diamond crystal growth technology, diamond Raman lasers (DRLs) have shown significant advantages in achieving wavelength expansion with both high beam quality and high-power operation. However, with the output power of DRLs reaching the kilowatt level, the adverse effect of the thermal impact on the beam quality is progressively worsening. Aiming to enunciate the underlying restrictions of the thermal effects for high-power DRLs (e.g., recently reported 1.2 kW), we here establish a thermal-structural coupling model, based on which the influence of the pump power, cavity structure, and crystal size have been systematically studied. The results show that a symmetrical concentric cavity has less thermal impact on the device than an asymmetrical concentric cavity. Under the ideal heat dissipation condition, the highest temperature rise in the diamond crystal is 23.4 K for an output power of ~2.8 kW. The transient simulation further shows that the heating and cooling process of DRLs is almost unaffected by the pump power, and the times to reach a steady state are only 1.5 ms and 2.5 ms, respectively. In addition, it is also found that increasing the curvature radius of the cavity mirror, the length and width of the crystal, or decreasing the thickness of the crystal is beneficial to alleviating the thermal impact of the device. The findings of this work provide some helpful insights into the design of the cavity structure and heat dissipation system of DRLs, which might facilitate their future development towards a higher power.

Keywords: diamond; thermal effect; high power; thermal-structural coupling model

check for updates

Citation: Gong, Q.; Zhang, M.; Lin, C.; Yang, X.; Fu, X.; Ma, F.; Hu, Y.; Dong, L.; Shan, C. Analysis of Thermal Effects in Kilowatt High Power Diamond Raman Lasers. *Crystals* **2022**, *12*, 1824. https://doi.org/10.3390/cryst12121824

Academic Editor: Dah-Shyang Tsai

Received: 27 November 2022
Accepted: 12 December 2022
Published: 14 December 2022

Publisher's Note: MDPI stays neutral with regard to jurisdictional claims in published maps and institutional affiliations.

Copyright: © 2022 by the authors. Licensee MDPI, Basel, Switzerland. This article is an open access article distributed under the terms and conditions of the Creative Commons Attribution (CC BY) license (https://creativecommons.org/licenses/by/4.0/).

1. Introduction

High-power lasers with high beam quality have extensive applications in fields such as industrial processing, eye-safe lidar, laser medicine, military countermeasures, laser satellite communications, space exploration, etc. [1–7]. Raman lasers have received much attention in developing high-beam quality and high-power operation lasers because they can achieve beam purification by using unique automatic phase-matching characteristics [8]. Diamond crystal is considered an ideal material for Raman lasers with both high-power and good beam quality due to its high Raman gain coefficient (1332.3 cm^{-1}), low Raman linewidth (1.5 cm^{-1}), low thermal expansion coefficient (1.1 $\times$ 10^{-6} K^{-1}), high damage threshold, and thermal conductivity (2200 $Wm^{-1}K^{-1}$) that is 2–3 orders of magnitude higher than other crystals materials [8–11].

With continual developments in the chemical vapor deposition (CVD) manufacturing process of large-size single-crystal diamonds, diamond Raman lasers (DRLs) with both

high power and high beam quality have made remarkable progress in the last decade or so [8,11–24]. In 2014, the Mildren's group at Macquarie University reported a first-order Stokes light output with a power of 108 W. This is the first time that the output power of DRLs has reached the 100-watt scale with an optical-optical conversion efficiency of 34% and a beam quality factor of $M^2 < 1.1$ [25]. In 2018, they obtained a second-order Stokes light output of 302 W with an optical-optical conversion efficiency of 36% and a beam quality factor of $M^2 = 1.1$ [26]. In 2019, they further got the stokes light output of the kilowatt level (1.2 kW) with an optical-optical conversion efficiency of 53% and a beam quality factor of $M^2 = 1.25$ [27]. Despite these significant advances, it can be seen that the beam quality of the laser begins to deteriorate as the output power of DRLs reaches the kilowatt level, indicating that the adverse effect of the thermal impact on the beam quality is progressively increasing.

Part of the energy for the pump light is converted into heat in the crystal, causing a temperature rise that is the root cause of the thermal effects [28–33]. The uneven temperature distribution inside the laser crystal will cause uneven expansion inside the medium and generate thermal stress to deform the crystal, resulting in a decrease in the conversion efficiency of the pumped light inside the crystal. It is generally believed that the configuration of the laser resonant cavity, the power and beam distribution of the pump light, the size of the laser crystal, as well as the heat dissipation method and the structure of the heat dissipation system are important factors affecting the thermal effect of the laser crystal [34–39].

Up to now, there has been a lack of research on the thermal effects of DRLs because the excellent thermal conductivity of diamond allows the neglect of its thermal effects for low input power. However, the thermal effects of the diamond play a key role in limiting the output power and beam quality of the laser when the output power of DRLs reaches the hundred-watt or even kilowatt level [6,40–42]. In 2021, Bai et al. studied the thermal effects of DRLs by using a simpler point source as a heat source model and found that the temperature rise of the device reached 70 K at an output power of 302 W [40]; recently, the group further found that the temperature rise of the device was only 7.15 K at an output power of 132 W by using the heat source model with crystal internal heat transfer, which is in better agreement with the experimental results [41]. These results provide a more significant contribution to the preliminary understanding of the thermal effects of DRLs. However, we note that there is a lack of research on the thermal effects of high-power DRLs for the kW level and a lack of research and understanding of the conformational relationship between cavity structure and thermal effects.

In this paper, aiming to discuss the fundamental limits of the thermal effects for high-power devices (e.g., 1.2 kW as recently reported [27]), we here establish a thermal-structural coupling model, based on which we first studied the relationship between device thermal effect and pump power; then, the influence of cavity structure, including cavity type, cavity mirror radius of curvature, and diamond size is further discussed. The results show that: (1) a symmetrical concentric cavity has less thermal impact on the device than an asymmetrical concentric cavity; (2) the maximum temperature rise in the crystal is ~23.4 K for DRLs with a symmetric concentric cavity at an output power of ~2.8 kW under the ideal heat dissipation condition; meanwhile, the warming and cooling processes of the device are fast, the heating and cooling processes of DRLs are almost unaffected by the pump power, and the times to reach a steady state are only ~1.5 ms and ~2.5 ms, respectively; (3) increasing the radius of curvature of the cavity mirror, increasing the length and width of the diamond crystal, or reducing the thickness of the crystal are all beneficial to the improvement of the thermal effect of the device. The results of this paper can help to deepen the understanding of the constitutive relationship of thermal effects for DRLs with high power and might provide some insights into the design of cavity structures and heat dissipation systems.

2. System Structure and Heat Source Model

According to the literature [27], we first built the cavity structure of DRLs as shown in Figure 1a, where the diamond crystals with dimensions of 1.2 mm × 4 mm × 8.6 mm are placed in a nearly concentric cavity consisting of concave mirrors with radii of curvature of 150 mm and 92 mm, respectively. The DRLs are pumped by a 1064 nm Nd: YAG laser, the device achieves a maximum output power of 1.2 kW, and an optical-to-optical conversion efficiency of 52.2% for a pump power of 2.3 kW. The system uses single-side water cooling, where the diamond is placed on a copper heat sink with dimensions of 3 mm × 8.6 mm × 8.6 mm (Figure 1b). Most of the heat inside the crystal is removed through a temperature control device (298 K) and water circulation inside it, while the rest of the heat is removed through heat exchange with air on the remaining five sides of the crystal. Here, we consider the ideal heat dissipation case, i.e., a constant temperature of 298 K at the bottom of the diamond crystal (also the upper surface of the copper heat sink).

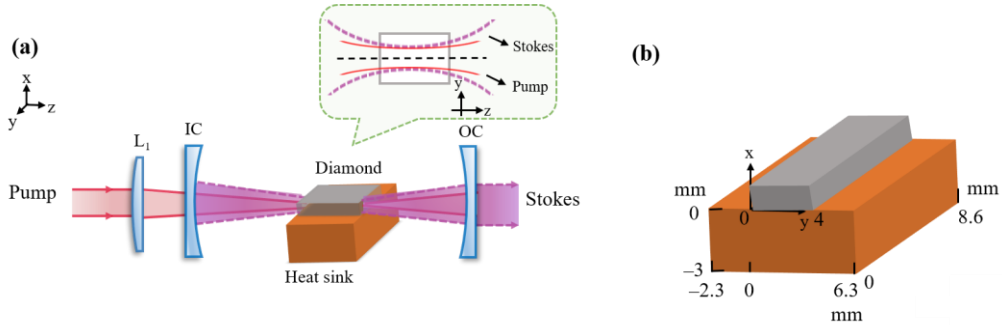

Figure 1. (**a**) Schematic of DRLs used for the simulation. (**b**) Model of the diamond crystal and copper heat sink used for the simulation.

2.1. Thermal Model of Diamond Crystal

In this work, we use a Gaussian heat source model that is closer to the actual pump beam characteristics than the point heat source model, which is widely accepted in solid-state laser heat dissipation studies [28,31,36,43]. The pump light is assumed to be approximated as a Gaussian beam, which is focused through the lens to the center of the diamond crystal. Meanwhile, assuming that the pump beam waist radius is equal to the Stokes beam waist radius due to the consideration of the requirement of good mode matching [26,40,44], the heat source function can then be expressed as:

$$Q_v(x,y,z) = \frac{2\xi P_{pump}}{\pi\omega_p^2 l} exp\left[-2\frac{\left(x-\frac{a}{2}\right)^2+\left(y-\frac{b}{2}\right)^2}{\omega_p^2}\right] exp(-\alpha z) \quad 0 \le x \le a,\ 0 \le y \le b,\ 0 \le z \le l \tag{1}$$

$$\xi = 1 - \eta \tag{2}$$

$$\omega_p = \omega_0\sqrt{1+\left(\frac{\left(z-\frac{l}{2}\right)}{z_p}\right)^2} \tag{3}$$

$$z_p = \frac{\pi n \omega_0^2}{M^2\lambda_p} \tag{4}$$

where a, b, and l are the thickness, width, and length of the diamond crystal, respectively, P_{pump} is the pump power of the laser, z_p is the Rayleigh length, ω_0 is beam radius of the pump light, ω_p is the beam waist radius of the pump light at any position within the crystal, as shown in Table 1, α is the absorption coefficient of the diamond crystal, ξ is the thermal conversion coefficient, $\eta = \lambda_p/\lambda_s$ is the quantum conversion efficiency, λ_p, λ_s are the wavelengths of the pump light and Stokes light, respectively, and n is the refractive index of the diamond crystal.

Table 1. Parameters used in simulation.

	Parameters	Value
Diamond	Thermal conductivity K	2000 $Wm^{-1}K^{-1}$
	Coefficient of thermal expansion α_T	1.1×10^{-6} K^{-1}
	Absorption coefficient α	0.375 m^{-1}
	Thermal coefficient of the refractive index d_n/d_t	1.5×10^{-5} K^{-1}
	Thermal conversion coefficient ξ	0.142
	Density	3510 kgm^{-3}
	Crystal refractive index n	2.39 @1 μm
	Crystal size	1.2 mm × 4 mm × 8.6 mm
	Young's modulus	1100 GPa
	Poisson's ratio ν	0.069
Copper	Size	3 mm × 8.6 mm × 8.6 mm
	Thermal conductivity	385 $Wm^{-1}K^{-1}$
DRLs	Pump wavelength λ_p	1064 nm
	Quality factor of pumping beam M_p^2	15
	Stokes wavelength λ_s	1240 nm
Water	Constant temperature	298 K (25 °C)
Air	Ambient temperature T_0	298 K (25 °C)

Assuming that the thermal conductivities of diamond crystals in the x, y, and z directions are k_x, k_y, and k_z, respectively, the three-dimensional heat conduction equation is [29–31]:

$$k_x \frac{\partial^2 T(x,y,z)}{\partial x^2} + k_y \frac{\partial^2 T(x,y,z)}{\partial y^2} + k_z \frac{\partial^2 T(x,y,z)}{\partial z^2} + Q_v(x,y,z) = 0$$
$$0 \le x \le a,\ 0 \le y \le b,\ 0 \le z \le l \tag{5}$$

where $T(x,y,z)$ is the temperature at any point position within the crystal. At the beginning of heating, the initial moment conditions are set assuming that the diamond crystal and the copper heat sink are in equilibrium as follows:

$$T(x,y,z,0) = T_0 \tag{6}$$

T_0 is the external ambient temperature, where the natural convection of air and the radiation of the thermal environment between the diamond and the copper heat sink and the surrounding environment are taken into account during the heating process.

2.2. Thermo-Elasticity Model of Diamond Crystal

When the pump light hits the crystal, part of the energy is absorbed, and the rest of the power is converted into heat unevenly distributed inside the crystal, which leads to uneven temperature distribution, resulting in uneven thermal expansion in the crystal. The magnitude of thermal stresses and thermal strains caused by the uneven temperature variations in the crystal can be solved by coupled thermal-stress analysis, i.e., the thermal analysis of the diamond crystal is first performed, and the mechanical analysis is performed based on the results of the thermal analysis simulation, where the position and stress state of the crystal is determined by a set of thermoelastic equations, including geometric, physical, and equilibrium differential equations [31,40,41], as follows:

Firstly, the relationship between strain and displacement can be described by the geometric equation, which is as follows:

$$\begin{cases} \varepsilon_x = \frac{\partial u_x}{\partial x}, \varepsilon_y = \frac{\partial u_y}{\partial y}, \varepsilon_z = \frac{\partial u_z}{\partial z} \\ \varepsilon_{xy} = \frac{\gamma_{xy}}{2} = \frac{1}{2}\left(\frac{\partial u_x}{\partial y} + \frac{\partial u_y}{\partial x}\right) \\ \varepsilon_{yz} = \frac{\gamma_{yz}}{2} = \frac{1}{2}\left(\frac{\partial u_y}{\partial z} + \frac{\partial u_z}{\partial y}\right) \\ \varepsilon_{zx} = \frac{\gamma_{zx}}{2} = \frac{1}{2}\left(\frac{\partial u_z}{\partial x} + \frac{\partial u_x}{\partial z}\right) \end{cases} \tag{7}$$

where u_x, u_y, u_z are the displacement components of the crystal in the x, y, and z directions, respectively, ε_x, ε_y, and ε_z are the line strain components of the crystal in the x, y, and z directions, respectively, and γ_{xy}, γ_{yz}, and γ_{zx} are the shear strain components of the crystal in the three planes, respectively.

Secondly, the relationship between stress and strain satisfies Hooke's law and can be described by the physical equation:

$$\begin{cases} \varepsilon_x = \frac{\partial u_x}{\partial x} = \frac{1}{E}\left[\sigma_x - \mu\left(\sigma_y + \sigma_z\right)\right] + \alpha_T \Delta T \\ \varepsilon_y = \frac{\partial u_y}{\partial y} = \frac{1}{E}\left[\sigma_y - \mu\left(\sigma_z + \sigma_x\right)\right] + \alpha_T \Delta T \\ \varepsilon_z = \frac{\partial u_z}{\partial z} = \frac{1}{E}\left[\sigma_z - \mu\left(\sigma_x + \sigma_y\right)\right] + \alpha_T \Delta T \end{cases} \tag{8}$$

$$\gamma_{xy} = \frac{\tau_{xy}}{G}, \gamma_{yz} = \frac{\tau_{yz}}{G}, \gamma_{zx} = \frac{\tau_{zx}}{G} \tag{9}$$

σ_x , σ_y, σ_z are the stress components of the crystal in the x, y, and z directions, respectively, μ is the Poisson's ratio, E is the tensile modulus of the crystal, α_T is the coefficient of the thermal expansion of the crystal, ΔT is the temperature change, and $G = \frac{E}{2(1+\mu)}$, is the shear modulus of elasticity.

The crystal satisfies the hydrostatic equilibrium condition when a diamond crystal is in equilibrium:

$$\Sigma X = \Sigma Y = \Sigma Z = \Sigma M_x = \Sigma M_y = \Sigma M_z = 0 \tag{10}$$

Using the equilibrium condition for the moments $\Sigma M_x = \Sigma M_y = \Sigma M_z = 0$, we can obtain:

$$\begin{cases} \tau_{xy} = \tau_{yx} \\ \tau_{xz} = \tau_{zx} \\ \tau_{yz} = \tau_{zy} \end{cases} \tag{11}$$

Using the displacement equilibrium condition $\Sigma X = \Sigma Y = \Sigma Z = 0$, we can obtain the equilibrium differential equations for the forces in the x, y, and z directions of the crystal, respectively, as:

$$\begin{cases} \frac{\partial \sigma_x}{\partial x} + \frac{\partial \tau_{yx}}{\partial y} + \frac{\partial \tau_{zx}}{\partial z} + F_x = 0 \\ \frac{\partial \tau_{xy}}{\partial x} + \frac{\partial \sigma_y}{\partial y} + \frac{\partial \tau_{zy}}{\partial z} + F_y = 0 \\ \frac{\partial \tau_{xz}}{\partial x} + \frac{\partial \tau_{yz}}{\partial y} + \frac{\partial \sigma_z}{\partial z} + F_z = 0 \end{cases} \tag{12}$$

where, F_x, F_y, F_z are the external force components acting on the diamond crystal in x, y, and z directions, respectively, and $F_x = F_y = F_z = 0$ since the surface of the diamond crystal is freely bounded. Bringing Equations (8) and (9) into Equation (12), the equilibrium differential equation expressed in terms of displacement components can be obtained.

2.3. Thermal Lensing Strength of Diamond Crystal

A large heat load is accumulated in diamond crystal due to the attenuation of the optical phonons generated by Raman and the absorption of impurities or defects in the crystal by pump light and Stokes light from DRLs. The heat generated affects the conversion efficiency and beam quality of DRLs through the thermal lensing effect, thermally induced stress birefringence, and thermally induced stress fracture, where the thermal lensing effect

is one of the critical parameters in the study of thermal effects. To evaluate the effect of thermal lensing inside the crystal, the magnitude of the thermal lensing intensity within the crystal can be calculated. Assuming a uniform thermal accumulation along the length of the crystal as P_h, the thermal lens intensity is mainly influenced by the thermally induced radial perturbation of the refractive index, end-face bulging, and photo-elastic effects, which can be expressed as the equation of the intensity as [6,45,46]:

$$f^{-1} \approx \frac{P_h}{2\pi\omega_p^2 K} \cdot \left(d_n/d_t + (n-1)(\nu+1)\alpha_T + n^3\alpha_T C_{r,\varphi} \right) \tag{13}$$

$$P_h = \xi P_{dep} + \alpha_p P_{pump} + \alpha_s P_s/(1-R_s) \tag{14}$$

As shown in Table 1, where K is the thermal conductivity of the diamond, d_n/d_t is the thermo-optical coefficient of the refractive index, n is the refractive index of the diamond crystal, ν is the Poisson's ratio, α_T is the coefficient of thermal expansion, $C_{r,\varphi}$ is the photoelasticity coefficient, where P_{dep} is the heat deposited (per unit time) due to the production of Raman phonons and absorption of the Stokes beam, and P_{pump} is the pump power of the laser. In this work, we assumed that $P_{dep} = P_{pump}$, which is more convenient for our calculations. P_s is the output power of Stokes light; α_p and α_s are the absorption coefficients of the diamond crystal for pump light and Stokes light, respectively. Since the wavelength difference between pump light and Stokes light is insignificant, it is assumed that $\alpha_p = \alpha_s$ (0.375 m^{-1} @1 μm), and R_s is the reflectance of the output coupling mirror to Stokes light.

For diamond crystals, since the thermo-optical effect is several orders of magnitude higher than the photo-elastic effect [24], under the first-order approximation, only the thermo-refractive index change is usually calculated, while neglecting the effect of the last two terms in Equation (13), so the thermal lensing intensity of the crystal can be simplified as:

$$f^{-1} \approx \frac{P_h}{2\pi\omega_p^2 K} \cdot d_n/d_t \tag{15}$$

Thus, the thermal lensing intensity of the crystal is proportional to the pump power; the higher the pump power, the more serious the thermal lensing effect; inversely proportional to the square of the pump spot radius, the larger the pump spot, the smaller the thermal lensing effect.

3. Results and Discussion

3.1. The Effect of Pump Power on Thermal Effect

3.1.1. Temperature Distribution at Different Pumping Power Levels

Firstly, we examine the steady-state temperature distribution inside the diamond crystal for different pump power levels. Due to the optical-to-optical conversion efficiency being 52.2% [27], when pump power levels are 800 W, 2.3 kW, 3.8 kW, and 5.3 kW, respectively, the corresponding output power levels would be about 0.42 kW, 1.2 kW, 2.0 kW, and 2.8 kW. As shown in Figure 2, the temperature variation of the diamond crystal is mainly concentrated in the pumped region, i.e., near the central crystal axis. With the pumping power rising from 800 W to 5.3 kW, the maximum temperature rise inside the crystal gradually increases from 3.2 K to 23.4 K. In the transverse direction (y-direction), the temperature distribution inside the crystal is symmetrical, and it gradually decreases from the center to both sides of the face. Finally, both sides of the surface and ambient temperature are almost the same.

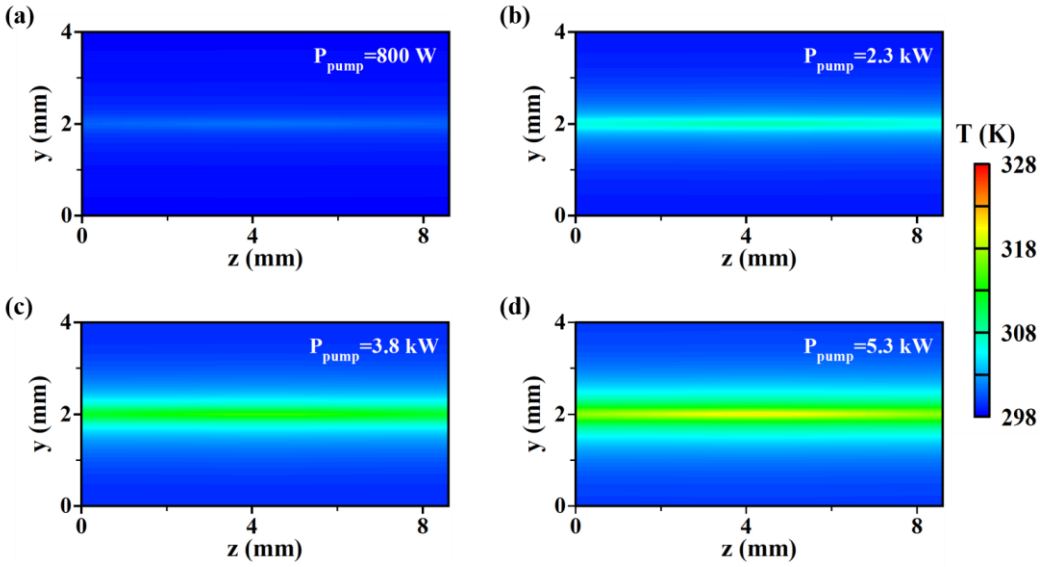

Figure 2. Cross-sectional temperature distribution of diamond crystal at pumping power (**a**) 800 W (**b**) 2.3 kW (**c**) 3.8 kW, and (**d**) 5.3 kW, respectively.

Figure 3 further gives the temperature variations in three directions inside the diamond for different pumping power levels. It can be seen from Figure 3a that the temperature is highest at the center of the crystal on the lateral side [31,41], and the temperature difference between the center temperature and the lateral edge increases gradually from 3.2 K to 21.5 K as the pumping power increases. From Figure 3b, it can be seen that the temperature also decreases gradually from the center of the crystal to the two end faces in the crystal axis direction, with the lowest temperature at the two ends, which is because the pump beam waist position coincides with the center of the diamond crystal so that the pump energy density is the largest, and at the same time, both ends of the crystal are in contact with the air, so the heat dissipation effect is better than the center of the crystal, which is consistent with the findings in the Ref. [47]. With the pumping power increasing from 800 W to 5.3 kW, the temperature gradient between the center of the crystal and the two end faces increases from 0.6 K to 4.0 K. Figure 3c shows the temperature distribution along the x-direction (thickness direction) at the central face of the crystal. It can be seen that the highest temperature also occurs at the central position of the crystal, which is 301.5 K, 308.1 K, 314.8 K, and 321.4 K at the pump power of 800 W, 2.3 kW, 3.8 kW, and 5.3 kW, respectively. The temperature decreases gradually from the center of the crystal to the upper and lower surfaces. Since the bottom surface of the diamond crystal is in contact with the copper heat sink and is fixed at the ideal 298 K, its heat dissipation effect is better than that of the upper surface. The temperature decreases rapidly from the center of the crystal to 298 K, while the temperature of the upper surface increases with the increase in pumping power.

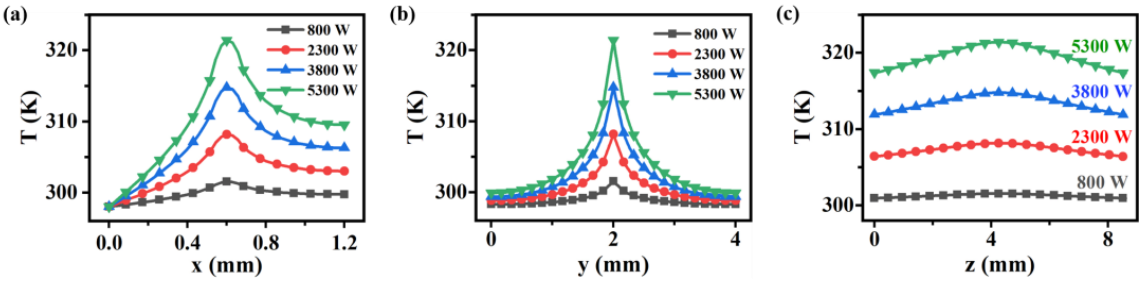

Figure 3. Temperature distribution of (**a**) x-axis intercept in crystal center plane, (**b**) y-axis intercept in crystal center plane, and (**c**) crystal axis at different pumping power levels.

It should be noted that the temperature of the bottom surface of the diamond crystal (or the top of the copper heat sink) is assumed to be constant at 298 K in this work, which is an ideal state, while if the temperature at the bottom of the copper heat sink is fixed at 298 K, the maximum temperature inside the diamond crystal will reach 355.7 K at a pump power of 2.3 kW. The corresponding maximum temperature rise will be significantly increased from 10.1 K to 57.7 K, which is even much higher than the ideal case with a pump power of 5.3 kW. This shows that it is crucial for DRLs to rationally design the heat dissipation structure of the diamond crystal.

We further investigated the warming process of the diamond crystal in the case of pulsed pumping and the cooling process after stopping pumping. The results are shown in Figure 4. T_c and T_s are the temperatures of the diamond in the volume center and the upper surface center, respectively, $T_c - T_s$ is their temperature difference, and the time for the temperature gradient to reach 99% of the steady-state value is defined as the constant thermal time [25,40]. It can be seen from Figure 4a that the volume center temperature of the diamond crystal is higher and rises faster than the upper surface center temperature at the beginning stage after the pump pulse action, which is because the pump energy is concentrated at the center of the crystal. The upper surface center temperature starts to rise from ~0.01 ms. It stabilizes at about 1.5 m, during which the temperature of the volume center is always higher than the upper surface temperature of the crystal, which is consistent with the results of the steady-state temperature distribution within the diamond. It is worth noting that the thermal constant time is almost independent of the pumping power because the thermal equilibrium time is mainly determined by the pumping beam area and the basic thermal properties of the crystal (specific heat capacity and thermal conductivity) [25].

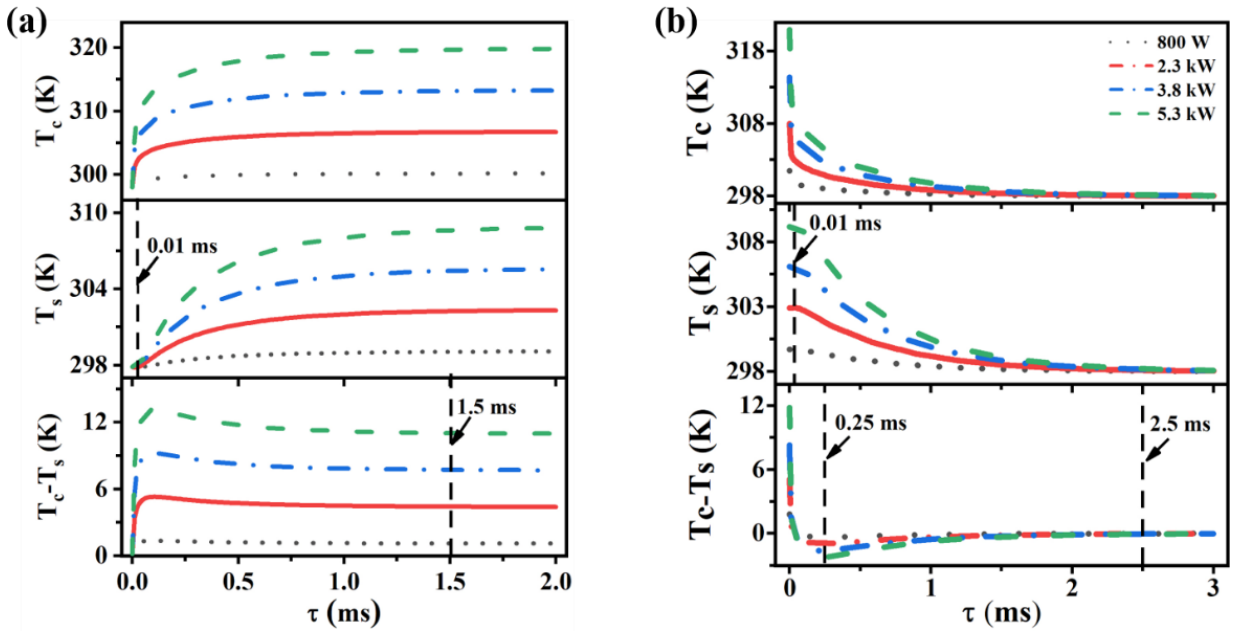

Figure 4. Transient temperature variation of diamond crystal at different pumping power levels during (**a**) heating and (**b**) cooling.

Figure 4b shows the results of the cooling process for the diamond crystal after the pumping stopped. Within 0.01 ms of removing the heat source, the center temperature of the upper surface of the diamond crystal remains almost unchanged. In contrast, the temperature of the volume center drops rapidly to be close to that of the upper surface. After that, the center temperature of the upper surface of the diamond crystal starts to decrease slowly. The hysteresis of the cooling is mainly caused by the different heat dissipation conditions on the upper and lower surfaces, which can also be seen from the variation of the temperature difference $T_c - T_s$: after the heat source is removed, the temperature

difference $T_c - T_s$ decreases rapidly, and becomes negative after ~0.01 ms, reaching the maximum value at ~0.25 ms, and then slowly converges to the ambient temperature (298 K). The thermal effect reaches equilibrium after the pumping stops after ~2.5 ms. Similarly, the time required to reach equilibrium finally is almost unaffected for different pump power levels, despite the slightly different range of temperature variations. Based on this result, we can speculate that kW-level Raman laser emission without heat accumulation can be achieved at repetition frequencies of ~250 Hz for the diamond crystals cooled on one side in this paper.

3.1.2. Thermal Stress Distribution under Different Pumping Power

Figure 5 shows the distribution of thermal stresses inside the diamond at different pumping power levels. It can be seen that the stress is highest at the center of the crystal and lowest at the center of both end faces, and the maximum thermal stress inside the crystal increases from 20.7 MPa to 137.4 MPa as the pumping power increases from 800 W to 5.3 kW. It is noteworthy that this distribution and trend of thermal stress is similar to the results of the temperature distribution inside the diamond (Figure 2), which is mainly because the higher thermal expansion at higher temperature locations within the crystal requires more stress generation to avoid thermal deformation. Also, due to the diamond having a smaller thermal expansion coefficient, this thermal stress is significantly lower than other crystals at the same pumping power level, such as Tm: YAP and Tm: LuAG et al. [31,36].

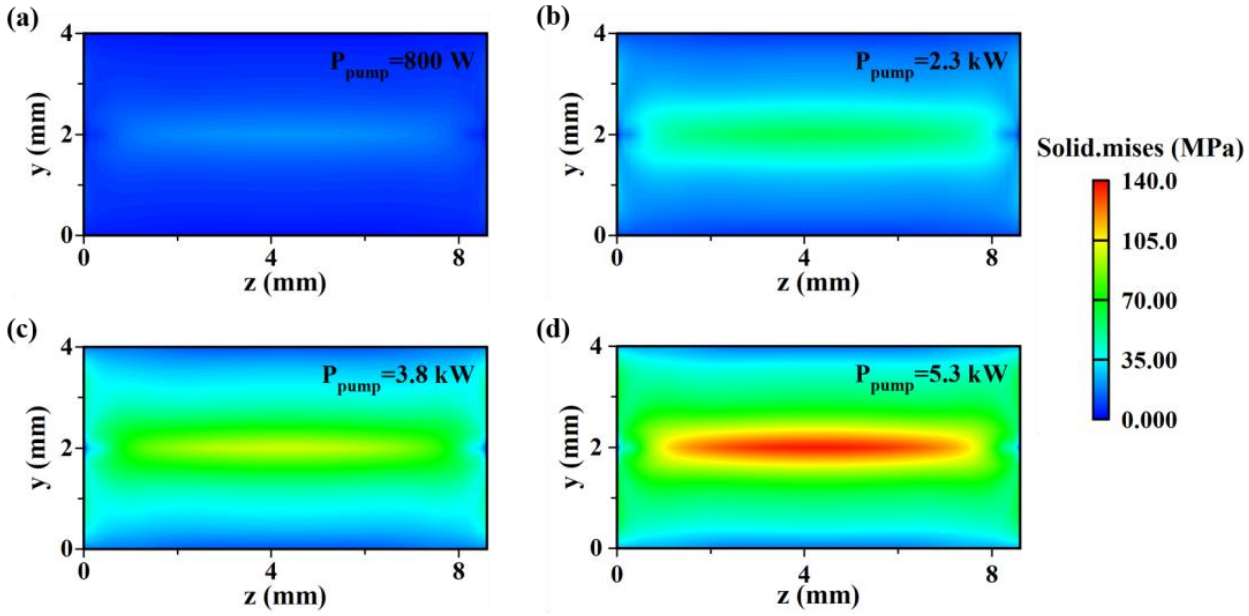

Figure 5. Cross-sectional thermal stress distribution of diamond crystal at different output power levels, (**a**) 800 W, (**b**) 2.3 kW, (**c**) 3.8 kW, and (**d**) 5.3 kW.

3.1.3. Heat Deformation Distribution under Different Pumping Power

According to Equation (8), the relationship between deformation and stress satisfies Hooke's law, i.e., thermal stress tends to prevent thermal deformation, which also means that the distribution of thermal deformation will be opposite to the distribution of thermal stress [41]. The corresponding results are given in Figure 6, where it can be seen that the deformation at the center of the crystal is the smallest, and the deformation at both ends is the largest for different pumping power levels. With the pumping power increasing from 800 W to 5.3 kW, the maximum deformation in the crystal increases from 0.02 μm to 0.13 μm. Nevertheless, this result is significantly lower than other crystal materials [31,36].

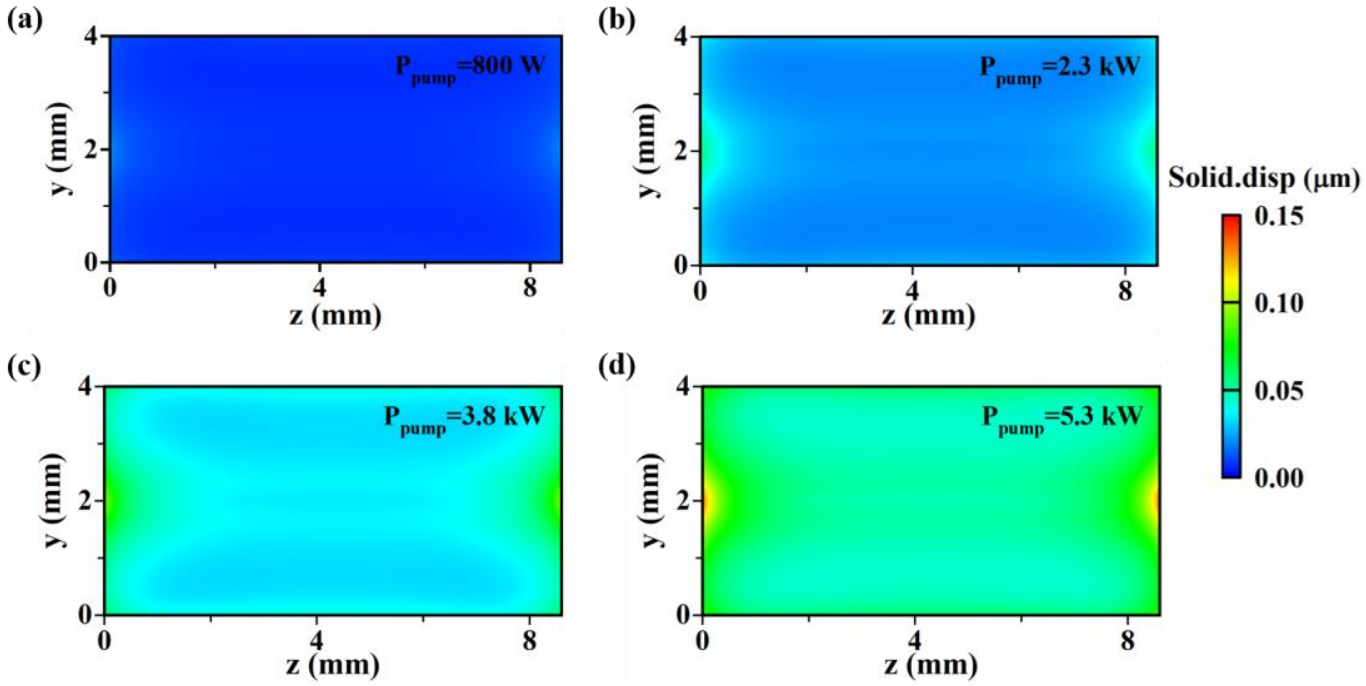

Figure 6. Cross-sectional thermal deformation distribution of diamond crystal at different output power levels, (**a**) 800 W, (**b**) 2.3 kW, (**c**) 3.8 kW, and (**d**) 5.3 kW.

3.2. Effect of Resonant Cavity Configuration on the Thermal Effects

To analyze the factors influencing the thermal effect more comprehensively, we further investigated the thermal impact of the devices at different cavity lengths and cavity curvature radii on the basis of the literature of [27] (pumping power of 2.3 kW). Considering the cavity lengths of 100 mm, 150 mm, 200 mm, and 250 mm, respectively, Figure 7a–d is the temperature distribution of the crystal axes at different cavity radii of curvature. It can be seen that the symmetric concentric cavity ($L = R1 + R2$) structures all exhibit the lowest crystal temperature for different cavity lengths, and the longer the cavity length (i.e., the larger the radius of curvature), the lower the temperature. The minimum temperatures for the four cavity lengths are 309.5 K, 308.7 K, 308.3 K, and 308.0 K, respectively. The above temperature distribution pattern is mainly caused by the variation of pump light energy density: the increase in cavity length and the radius of curvature of the cavity mirror causes the increase in the beam waist radius of the first-order Stokes light, which leads to the rise in the pump light beam waist radius (a requirement for good mode matching) so that the pump energy density decreases, and the temperature inside the crystal decreases. It is easy to calculate from the ABCD matrix to obtain the beam waist radii of Stokes light at four cavity lengths; they have slight variations, which are 66 μm, 73 μm, 78 μm, and 83 μm, respectively; therefore, the difference in minimum temperature is also tiny, only ~1.5 K.

Figure 7e,f summarizes the relationship between the maximum thermal stress and thermal deformation of the concentric cavity DRLs with the radius of cavity curvature for different cavity lengths, respectively. It can be seen that the maximum thermal stresses all gradually decrease with the increase in the radius of curvature of the cavity mirror for all four cavity lengths, but the overall effect is weak and eventually tends to stabilize at ~60 MPa. The maximum thermal deformations under different conditions (Figure 7f) are independent of the cavity length and radius of cavity curvature, which all remain around ~0.057 μm.

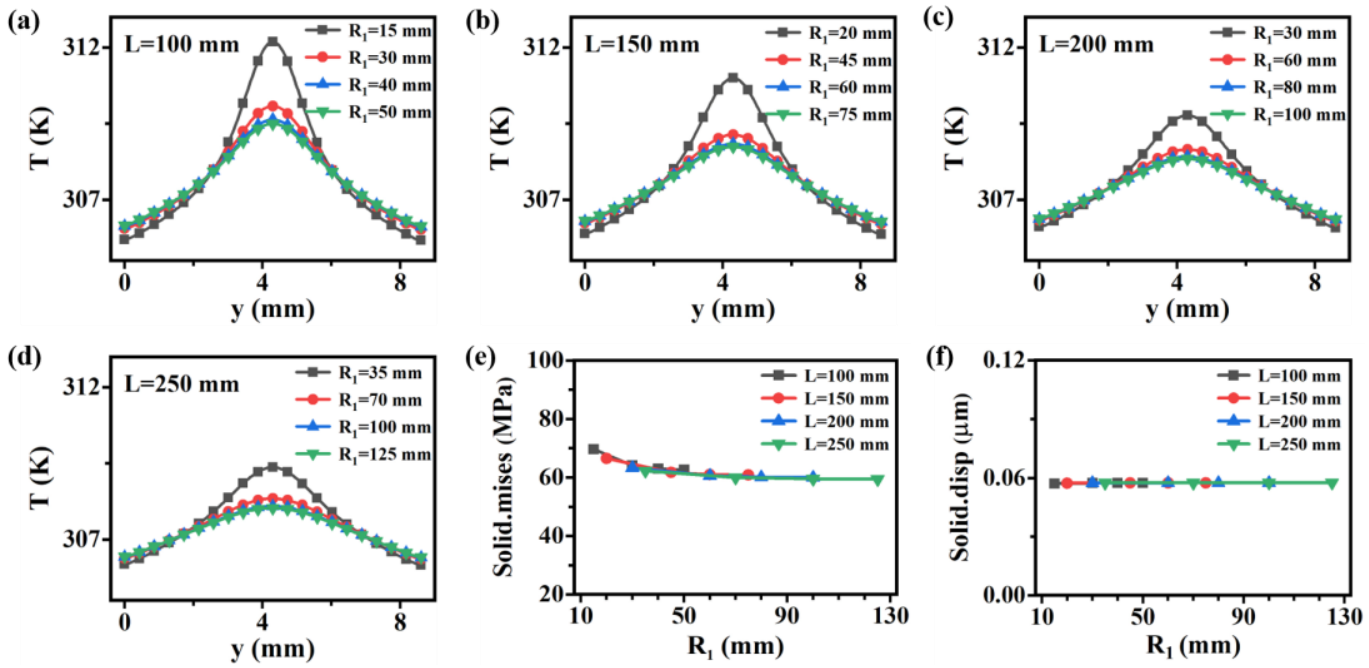

Figure 7. Cross-sectional temperature distribution of diamond crystal with concentric cavity of different radii of curvature at different cavity lengths, (**a**) 100 mm, (**b**) 150 mm, (**c**) 200 mm, and (**d**) 250 mm. Distribution of (**e**) maximum thermal stress, and (**f**) maximum thermal deformation inside crystals with a symmetrical concentric cavity at different radii of curvature.

3.3. Effect of Diamond Crystal Size on the Thermal Effect

Considering that the application of larger-size single-crystal diamonds will become possible in the future, we further discussed the effect of the diamond crystal size on thermal effects. Figure 8a shows the variation of the maximum temperature inside the diamond crystal (crystal cross-section is 1.2 mm × 4 mm) for different lengths. It can be seen that the maximum temperature inside the crystal gradually decreases from 310.1 K to 306.3 K as the crystal length increases from 7 mm to 11 mm. This is because the increase in crystal length will make the conversion of pump light to Stokes light more adequate, thus improving the utilization of pump light and reducing heat accumulation. Figure 8b shows the variation of maximum thermal stress with crystal length. It can be seen that the effect of crystal length on the maximum thermal stresses inside the crystal is negligible; they all remain around 60 MPa. In contrast, the ultimate thermal deformation gradually decreases from 0.07 μm to 0.04 μm as the crystal length increases (Figure 8c). Figure 8d shows the relationship between the maximum temperature inside the diamond crystal and the width and thickness of the crystal for a fixed length of 8.6 mm. It can be seen that the maximum temperature increases with the increase in the crystal thickness when the width of the crystal is certain; this is because the bottom of the diamond is fixed at 298 K, and increasing the thickness of the diamond is equivalent to increasing the distance between the heat source and the heat sink, which indicates that the thermal effect of DRLs increases with the increase in the crystal thickness; it is consistent with the findings of the literature [48] regarding the effect of the thickness of the Ti: Sa crystal on the thermal effect of the laser system; meanwhile, the maximum temperature decreases with increasing the width of the crystal when the thickness of the crystal is fixed, which is because expanding the width is equivalent to increasing the contact area between the diamond and the heat sink. Figure 8e shows the corresponding maximum thermal stresses. It can be seen that the maximum thermal stress of the device decreases slightly with increasing crystal width, and the effect of crystal thickness on the maximum thermal stress is negligible. Figure 8f shows the maximum thermal deformation as a function of crystal size. It can be seen that it tends to follow the same trend as the temperature change, where the thermal deformation decreases as the

crystal width increases, and the smaller the crystal thickness is, the smaller the thermal deformation is.

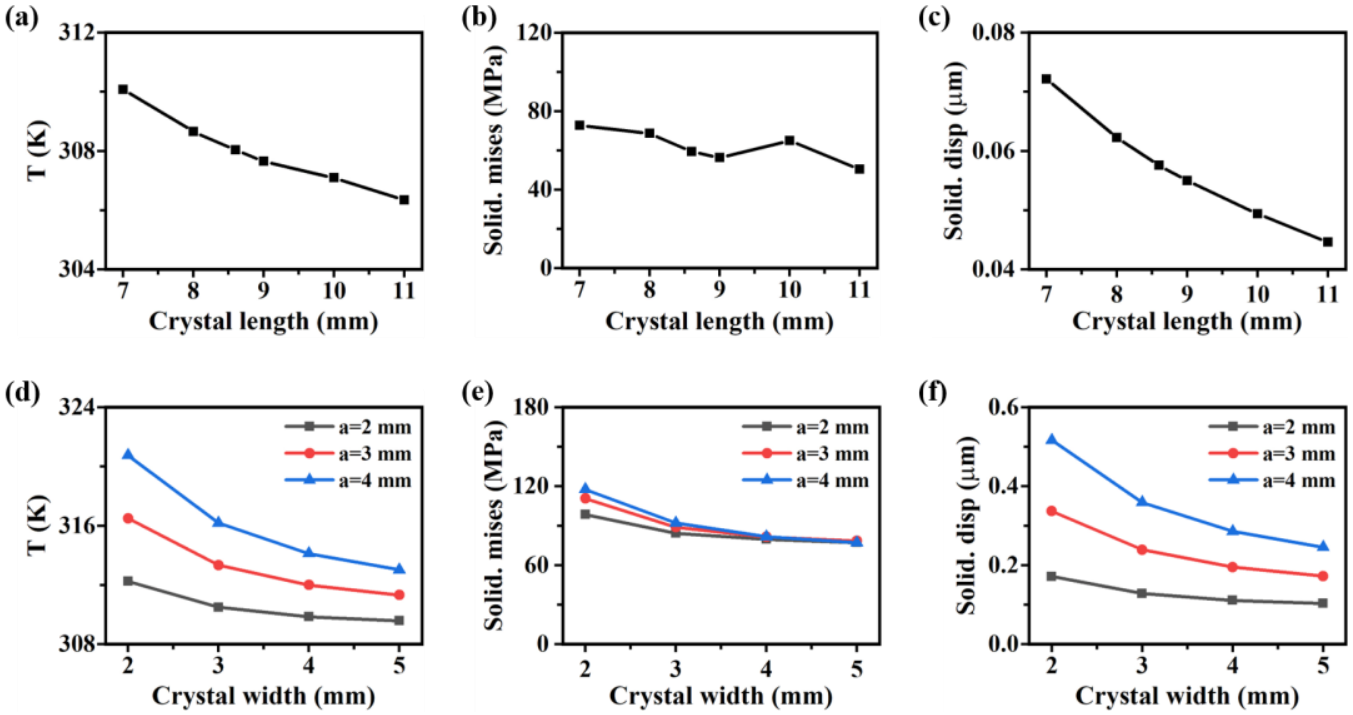

Figure 8. Distribution of (**a**) maximum temperature, (**b**) maximum thermal stress, and (**c**) maximum thermal deformation inside diamond crystals of different lengths. Distribution of (**d**) maximum temperature, (**e**) maximum thermal stress, and (**f**) maximum thermal deformation inside the diamond crystal for different crystal widths and thicknesses.

3.4. Thermal Lensing Effect Analysis

Finally, we discuss the variation of the thermal lens strength of DRLs with the pump power for different cavity radii of curvature (symmetric concentric cavity) and crystal lengths. It can be seen from Figure 9a that the thermal lens strength decreases with increasing the cavity radius of curvature when the pumping power is constant because an increase in the radius of curvature of the cavity mirror will cause an increase in the radius of the first-order Stokes beam waist and a consequent increase in the pump beam waist, which will lead to a decrease in the temperature rise in the crystal and, consequently, a decrease in the refractive index change. It can also be seen from Figure 9a that the thermal lens strength increases significantly with the increase in the pumping power, indicating that the rise of the pumping power causes the thermal accumulation of the crystal to increase rapidly, which in turn leads to the rapid change of the refractive index. However, with the pump power increasing, the thermal lens strength increases more flatly for structures with a large cavity radius of curvature. When the pump power increases to 5300 W and the cavity radii of curvature are 50 mm, 75 mm, 100 mm, and 125 mm, respectively, the thermal lens strengths are 163.6 m^{-1}, 133.7 m^{-1}, 117.1 m^{-1}, and 103.5 m^{-1}, which are similar to the thermal lens strength of diamond crystal in the literature [6,45], while significantly lower than those of other crystals such as Nd: $GdVO_4$ and Tm: YLF [34,35]. There is a similar conclusion for different crystal lengths (Figure 9b), where the thermal lens strength decreases with increasing pump power and crystal length.

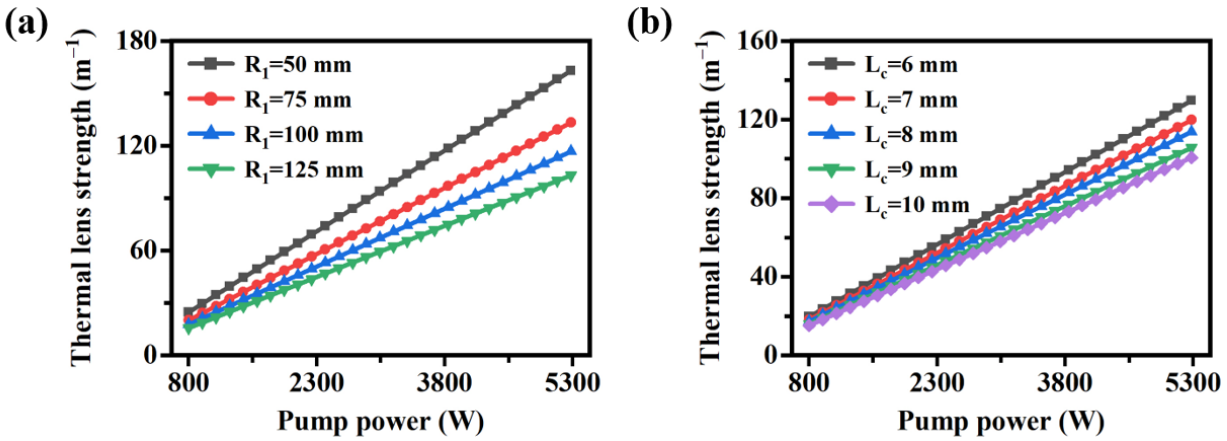

Figure 9. Relationship between thermal lens intensity and pump power at different (**a**) radii of curvature of cavity mirrors, and (**b**) crystal lengths.

4. Conclusions

In conclusion, aiming to discuss the fundamental limits of the thermal effects for high-power devices, we here establish a thermal-structural coupling model, based on which the influence of the pump power, cavity structure, and crystal size have been systematically studied. The results show that using a symmetric concentric cavity structure and increasing its radius of curvature, choosing the appropriate diamond size (increasing the length and width of the diamond crystal or decreasing the thickness of the crystal) is beneficial to alleviate the thermal effect of the device. Under ideal heat dissipation conditions, the maximum temperature rise in the crystal is ~23.4 K for DRLs, and the constant thermal times of the warming and cooling processes are ~1.5 ms and 2.5 ms, respectively, for an output power of ~2.8 kW. The results of this work provide a basis for the design of the resonant cavity structure of DRLs, which might promote the development of DRLs with high power and high beam quality.

Author Contributions: Conceptualization, Y.H.; methodology, Q.G., F.M. and L.D.; validation, C.L., X.Y. and X.F.; writing—original draft preparation, Q.G. and M.Z.; writing—review and editing, Y.H.; supervision, C.S.; funding acquisition, C.S. All authors have read and agreed to the published version of the manuscript.

Funding: This research was funded by the National Natural Science Foundation of China (NSFC) (Grant No. 11904323) and Research Funds of Zhengzhou University (Grant No. 32340305 and 32410543).

Data Availability Statement: Not applicable.

Conflicts of Interest: The authors declare no conflict of interest.

References

1. Lubin, P.; Hughes, G.B.; Bible, J.; Bublitz, J.; Arriola, J.; Motta, C.; Suen, J.; Johansson, I.; Riley, J.; Sarvian, N.; et al. Toward directed energy planetary defense. *Opt. Eng.* **2014**, *53*, 025103. [CrossRef]
2. Extance, A. Military technology: Laser weapons get real. *Nature* **2015**, *521*, 408–410. [CrossRef] [PubMed]
3. Meng, D.; Zhang, H.; Li, M.; Lin, W.; Shen, Z.; Zhang, J.; Fan, Z. Laser technology for direct IR countermeasure system. *Infrared Laser Eng.* **2018**, *47*, 1105009. [CrossRef]
4. Williams, R.J.; Spence, D.J.; Lux, O.; Mildren, R.P. High-power continuous-wave Raman frequency conversion from 1.06 μm to 1.49 μm in diamond. *Opt. Express* **2017**, *25*, 749–757. [CrossRef] [PubMed]
5. Bai, Z.; Williams, R.J.; Jasbeer, H.; Sarang, S.; Kitzler, O.; Mckay, A.; Mildren, R.P. Large brightness enhancement for quasi-continuous beams by diamond Raman laser conversion. *Opt. Lett.* **2018**, *43*, 563–566. [CrossRef] [PubMed]
6. Antipov, S.; Williams, R.J.; Sabella, A.; Kitzler, O.; Berhane, A.; Spence, D.J.; Mildren, R.P. Analysis of a thermal lens in a diamond Raman laser operating at 1.1 kW output power. *Opt. Express* **2020**, *28*, 15232–15239. [CrossRef] [PubMed]
7. McKay, A.; Kitzler, O.; Liu, H.; Fell, D.; Mildren, R.P. High average power (11 W) eye-safe diamond Raman laser. *SPIE* **2012**, *8551*, 115–122.

8. Jasbeer, H.; Williams, R.J.; Kitzler, O.; McKay, A.; Mildren, R.P. Wavelength diversification of high-power external cavity diamond Raman lasers using intracavity harmonic generation. *Opt. Express* **2018**, *26*, 1930–1941. [CrossRef]
9. Li, Y.; Bai, Z.; Chen, H.; Jin, D.; Yang, X.; Qi, Y.; Ding, J.; Wang, Y.; Lu, Z. Eye-safe diamond Raman laser. *Results Phys.* **2020**, *16*, 102853. [CrossRef]
10. Yang, X.; Kitzler, O.; Spence, D.J.; Bai, Z.; Feng, Y.; Mildren, R.P. Diamond sodium guide star laser. *Opt. Lett.* **2020**, *45*, 1898–1901. [CrossRef]
11. Williams, R.J.; Kitzler, O.; Bai, Z.; Sarang, S.; Jasbeer, H.; McKay, A.; Antipov, S.; Sabella, A.; Lux, O.; Spence, D.J.; et al. High power diamond Raman lasers. *IEEE J. Sel. Top. Quant.* **2018**, *24*, 1–14. [CrossRef]
12. Li, Y.; Ding, J.; Bai, Z.; Yang, X.; Li, Y.; Tang, J.; Zhang, Y.; Qi, Y.; Wang, Y.; Lu, Z. Diamond Raman laser: A promising high-beam-quality and low-thermal-effect laser. *High Power Laser Sci. Eng.* **2021**, *9*, 1–13. [CrossRef]
13. Mildren, R.P.; Sabella, A. Highly efficient diamond Raman laser. *Opt. Lett.* **2009**, *34*, 2811–2813. [CrossRef]
14. Spence, D.J.; Granados, E.; Mildren, R.P. Mode-locked picosecond diamond Raman laser. *Opt. Lett.* **2010**, *35*, 556–558. [CrossRef] [PubMed]
15. Lubeigt, W.; Bonner, G.M.; Hastie, J.E.; Dawson, M.D.; Burans, D.; Kemp, A.J. Continuous-wave diamond Raman laser. *Opt. Lett.* **2010**, *35*, 2994–2996. [CrossRef]
16. Sabella, A.; Piper, J.A.; Mildren, R.P. 1240 nm diamond Raman laser operating near the quantum limit. *Opt. Lett.* **2010**, *35*, 3874–3876. [CrossRef]
17. Parrotta, D.C.; Kemp, A.J.; Dawson, M.D.; Hastie, J.E. Tunable continuous-wave diamond Raman laser. *Opt. Express* **2011**, *19*, 24165–24170. [CrossRef]
18. Feve, J.P.M.; Shortoff, K.E.; Bohn, M.J.; Brasseur, J.K. High average power diamond Raman laser. *Opt. Express* **2011**, *19*, 913–922. [CrossRef]
19. Lubeigt, W.; Savitski, V.G.; Bonner, G.M.; Geoghegan, S.L.; Friel, I.; Hastie, J.E.; Dawson, M.D.; Burns, D.; Kemp, A.J. 1.6 W continuous-wave Raman laser using low-loss synthetic diamond. *Opt. Express* **2011**, *19*, 6938–6944. [CrossRef]
20. Savitski, V.G.; Reilly, S.; Kemp, A.J. Steady-State Raman Gain in Diamond as a Function of Pump Wavelength. *IEEE J. Quantum Electron.* **2013**, *49*, 218–223. [CrossRef]
21. McKay, A.; Liu, H.; Kitzler, O.; Mildren, R.P. An efficient 14.5 W diamond Raman laser at high pulse repetition rate with first (1240 nm) and second (1485 nm) Stokes output. *Laser Phys. Lett.* **2013**, *10*, 105801. [CrossRef]
22. Warrier, A.M.; Lin, J.; Pask, H.M.; Mildren, R.P.; Coutts, D.W.; Spence, D.J. Highly efficient picosecond diamond Raman laser at 1240 and 1485 nm. *Opt. Express* **2014**, *22*, 3325–3333. [CrossRef] [PubMed]
23. Wattiez, A.S.; Libert, F.; Privat, A.M.; Loiodice, S.; Fialip, J.; Eschalier, A.; Courteix, C. Evidence for a differential opioidergic involvement in the analgesic effect of antidepressants: Prediction for efficacy in animal models of neuropathic pain? *Br. J. Pharmacol.* **2011**, *163*, 792–803. [CrossRef] [PubMed]
24. Williams, R.J.; Nold, J.; Strecker, M.; Kitzler, O.; McKay, A.; Schreiber, T.; Mildren, R.P. Efficient Raman frequency conversion of high-power fiber lasers in diamond. *Laser Photonics Rev.* **2015**, *9*, 405–411. [CrossRef]
25. Williams, R.J.; Kitzler, O.; McKay, A.; Mildren, R.P. Investigating diamond Raman lasers at the 100 W level using quasi-continuous-wave pumping. *Opt. Lett.* **2014**, *39*, 4152–4155. [CrossRef]
26. Bai, Z.; Williams, R.J.; Kitzler, O.; Sarang, S.; Spence, D.J.; Mildren, R.P. 302 W quasi-continuous cascaded diamond Raman laser at 1.5 microns with large brightness enhancement. *Opt. Express* **2018**, *26*, 19797–19803. [CrossRef]
27. Antipov, S.; Sabella, A.; Williams, R.J.; Kitzler, O.; Spence, D.J.; Mildren, R.P. 1.2 kW quasi-steady-state diamond Raman laser pumped by an $M^2 = 15$ beam. *Opt. Lett.* **2019**, *44*, 2506–2509. [CrossRef]
28. Sun, R.; Wu, C.T.; Yu, M.; Yu, K.; Wang, C.; Jin, G.Y. Study on the laser crystal thermal compensation of LD end-pumped Nd: YAG 1319 nm/1338 nm dual-wavelength laser. *Laser Phys.* **2015**, *25*, 125004. [CrossRef]
29. Bai, F.; Huang, Z.; Liu, J.; Chen, X.; Wu, C.; Jin, G. Thermal analysis of double-end-pumped Tm: YLF laser. *Laser Phys.* **2015**, *25*, 075003.
30. Cui, J.; Liu, X.; He, L.; Zhang, S.; Yang, J. Investigation of the transient thermal profile of an anisotropic crystal in a pulsed and end-pumped laser. *J. Mod. Opt.* **2018**, *65*, 1847–1854. [CrossRef]
31. Zhang, H.; Wen, Y.; Zhang, L.; Zhen, F.; Liu, J.; Wu, C. Influences of Pump Spot Radius and Depth of Focus on the Thermal Effect of Tm: YAP Crystal. *Curr. Opt. Photonics* **2019**, *3*, 458–465.
32. Che, X.; Liu, J.; Wu, C.; Wang, R.; Jin, G. Thermal effects analysis of high-power slab Tm: YLF laser with dual-end-pumped based on COMSOL multiphysics. *Integr. Ferroelectr.* **2020**, *210*, 197–205.
33. Wang, K.; Fu, S.; Zhang, K.; Gao, M.; Gao, C. Thermal effects of the zig-zag Yb: YAG slab laser with composite crystals. *Appl. Phys. B* **2021**, *127*, 121. [CrossRef]
34. Nadimi, M.; Waritanant, T.; Major, A. Thermal lensing in Nd: $GdVO_4$ laser with direct in-band pumping at 912 nm. *Appl. Phys. B* **2018**, *124*, 170. [CrossRef]
35. Liu, J.L.; Chen, X.Y.; Yu, Y.J.; Wu, C.; Bai, F.; Jin, G. Analytical solution of the thermal effects in a high-power slab Tm: YLF laser with dual-end pumping. *Phys. Rev. A* **2016**, *93*, 013854. [CrossRef]
36. Wen, Y.; Wu, C.; Niu, C.; Zhang, H.; Wang, C.; Jin, G. Study on thermal effect of mid-infrared single-ended bonded Tm LuAG laser crystals. *Infrared Phys. Technol.* **2020**, *108*, 103356. [CrossRef]

37. Ren, T.; Zhao, L.; Fan, Z.; Dong, J.; Wu, C.; Chen, F.; Pan, Q.; Yu, Y. Transient thermal effect analysis and laser characteristics of novel Tm: LuYAG crystal. *Infrared Phys. Technol.* **2022**, *125*, 104238. [CrossRef]
38. Ramesh, K.N.; Sharma, T.K.; Rao, G. Latest advancements in heat transfer enhancement in the micro-channel heat sinks: A review. *Arch. Comput. Methods Eng.* **2021**, *28*, 3135–3165. [CrossRef]
39. Liu, S.; Xie, W.; Wang, Q.; Liu, Y.; Hu, N. Thermal performance of a central-jetting microchannel heat sink designed for a high-power laser crystal. *Int. J. Heat Mass Transf.* **2022**, *185*, 122409. [CrossRef]
40. Bai, Z.; Zhang, Z.; Wang, K.; Gao, J.; Zhang, Z.; Yang, X.; Wang, Y.; Lu, Z.; Mildren, R.P. Comprehensive thermal analysis of diamond in a high-power Raman cavity based on FVM-FEM coupled method. *Nanomaterials* **2021**, *11*, 1572. [CrossRef]
41. Ding, J.; Li, Y.; Chen, H.; Cai, Y.; Bai, Z.; Qi, Y.; Yan, B.; Wang, Y.; Lu, Z. Thermal modeling of an external cavity diamond Raman laser. *Opt. Laser Thchnol.* **2022**, *156*, 108578. [CrossRef]
42. Pashinin, V.P.; Ralchenko, V.G.; Bolshakov, A.P.; Ashkinazi, E.E.; Gorbashova, M.A.; Yorov, V.Y.; Konov, V.I. External-cavity diamond Raman laser performance at 1240 nm and 1485 nm wavelengths with high pulse energy. *Laser Phys. Lett.* **2016**, *13*, 065001. [CrossRef]
43. Chen, H.; Bai, Z.; Zhao, C.; Yang, X.; Ding, J.; Qi, Y.; Wang, Y.; Lu, Z. Numerical simulation of long-wave infrared generation using an external cavity diamond Raman laser. *Front. Phys.* **2021**, *9*, 671559. [CrossRef]
44. Kitzler, O.; McKay, A.; Mildren, R.P. High power CW diamond Raman laser: Analysis of efficiency and parasitic loss. In Proceedings of the 2012 Conference on Lasers and Electro-Optics (CLEO), San Jose, CA, USA, 6–11 May 2012.
45. Tu, H.; Ma, S.; Hu, Z.; Jiang, N.; Shen, Y.; Zong, N.; Yi, J.; Yuan, Q.; Wang, X.; Wang, J. Efficient monolithic diamond Raman yellow laser at 572.5 nm. *Opt. Mater.* **2021**, *114*, 110912. [CrossRef]
46. Huang, C.-Y.; Guo, B.-C.; Zheng, Z.-X.; Tsou, C.-H.; Liang, H.-C.; Chen, Y.-F. Continuous-Wave Crystalline Laser at 714 nm via Stimulated Raman Scattering and Sum Frequency Generation. *Crystals* **2022**, *12*, 1046. [CrossRef]
47. Qi, Y.; Zhang, Y.; Huo, X.; Wang, J.; Bai, Z.; Ding, J.; Li, S.; Wang, Y.; Lu, Z. Analysis on the thermal effect of Pr: YLF crystal for power scaling. *Opt. Eng.* **2022**, *61*, 046108. [CrossRef]
48. Chvykov, V. Ti: Sa Crystal Geometry Variation vs. Final Amplifiers of CPA Laser Systems Parameters. *Crystals* **2022**, *12*, 1127. [CrossRef]